nature sustainability

Article

https://doi.org/10.1038/s41893-024-01431-6

# Low-cost iron trichloride cathode for all-solid-state lithium-ion batteries

Received: 7 June 2023

Accepted: 15 August 2024

Published online: 23 September 2024

Check for updates

Zhantao Liu[1,7], Jue Liu[2,7], Simin Zhao[3], Sangni Xun[4], Paul Byaruhanga[5,6], Shuo Chen[5,6], Yuanzhi Tang[3], Ting Zhu[1] & Hailong Chen[1]

The dominant chemistries of lithium-ion batteries on the market today still rely on flammable organic liquid electrolytes and cathodes containing scarce metals, such as cobalt or nickel, raising safety, cost and environmental concerns. Here we show a $FeCl_3$ cathode that costs as little as 1% of the cost of a $LiCoO_2$ cathode or 2% of a $LiFePO_4$ cathode. Once coupled with a solid halide electrolyte and a lithium-indium (Li–In) alloy anode, it enables all-solid-state lithium-ion batteries without any liquid components. Notably, $FeCl_3$ exhibits two flat voltage plateaux between 3.5 and 3.8 V versus $Li^+/Li$, and the solid cell retains 83% of its initial capacity after 1,000 cycles with an average Coulombic efficiency of 99.95%. Combined neutron diffraction and X-ray absorption spectroscopy characterizations reveal a Li-ion (de)intercalation mechanism together with a $Fe^{2+}/Fe^{3+}$ redox process. Our work provides a promising avenue for developing sustainable battery technologies with a favourable balance of performance, cost and safety.

The increasing need for electrified transportation and grid power storage demands transformative electrochemical energy storage devices with a much lower cost than the currently used Li-ion batteries (LIBs)[1,2]. The cathode is responsible for a large part of the cost of a LIB. The materials currently used for the cathodes in commercial LIBs are mostly layered oxides, which are made from relatively expensive semi-precious raw materials[3], such as Co, and require costly processing, such as high-temperature calcination. Fe is an attractive redox-active element due to its low cost and low toxicity. Unfortunately, the layered oxide $LiFeO_2$ does not cycle in LIBs[4]. $LiFePO_4$ is less expensive than layered oxides in raw materials, but it commonly requires carbon coating and nanosizing[3,5,6], which increase the manufacturing cost and lowers the volumetric energy density.

Layered oxides usually react with Li through topotactic intercalation–deintercalation reactions, which are favourable for maintaining structural stability. In contrast, most binary compounds, such as transition-metal oxides[7–9] and halides[10–15], have been reported as being conversion cathodes or anodes in LIBs. They exhibit large voltage hysteresis[16] and low round-trip energy efficiency, which, thus, limit their application[17,18]. Only a small portion of the intercalation capacity of fluorides has been observed in $FeF_3$ (refs. 19–21) and FeOF (refs. 22–24). The reported Li intercalation plateau of $FeF_3$ varies from 3.0 to 3.3 V (refs. 19,25,26). Chlorides are, in principle, better hosts for Li intercalation than fluorides, as the bigger ions and weaker electronegativity of Cl than F may lead to faster diffusion channels in the lattice. However, most metal chlorides are soluble in commonly used organic liquid electrolytes (LEs), greatly limiting the use of chlorides as cathodes[27]. Only a limited number of studies have reported on chloride cathodes, most of which operate through conversion reactions and suffer from dissolution problems[11,13]. Recently, $VCl_3$ was reported to exhibit a $Li^+$ intercalation–deintercalation reaction when used in a saturated LE[28], but its cycling stability remains unsatisfactory.

Moreover, solid-state LIBs (SSLIBs), which use solid electrolytes (SEs) instead of conventional flammable LEs, are providing new opportunities. Besides the widely recognized benefits of solid-state batteries in terms of improved energy density, safety

[1]George W. Woodruff School of Mechanical Engineering, Georgia Institute of Technology, Atlanta, GA, USA. [2]Neutron Scattering Division, Oak Ridge National Laboratory, Oak Ridge, TN, USA. [3]School of Earth and Atmospheric Sciences, Georgia Institute of Technology, Atlanta, GA, USA. [4]School of Chemistry and Biochemistry, Georgia Institute of Technology, Atlanta, GA, USA. [5]Department of Physics, University of Houston, Houston, TX, USA. [6]Texas Center for Superconductivity, University of Houston, Houston, TX, USA. [7]These authors contributed equally: Zhantao Liu, Jue Liu.
e-mail: hailong.chen@me.gatech.edu

https://doi.org/10.1038/s41893-024-01431-6

and sustainability over conventional LIBs, using SEs also offers great opportunities for revisiting the chloride cathodes that are soluble in LEs. In particular, recent studies have shown that high-performance halide SEs[29–31], including our work on halides[32], exhibit good ionic conductivity and compatibility with high-voltage cathode materials. This progress suggests that there are opportunities for harnessing the combined benefits of stable $Li^+$ intercalation–deintercalation reactions in chloride cathodes and high-performance halide SEs for achieving high cycling stability.

Here we report that highly reversible Li insertion and extraction in anhydrous $FeCl_3$ in all-solid-state cells with halide SEs. $FeCl_3$ delivers an unexpectedly high voltage of ~3.65 V with a specific capacity of ~159 mAh $g^{-1}$ and an energy density of ~558 Wh $kg^{-1}$. More importantly, the market price of anhydrous $FeCl_3$ is only ~2% that of $LiFePO_4$, suggesting its huge potential for commercial applications in large-scale energy storage systems.

## Results

### Reversible Li insertion and extraction in $FeCl_3$

Pristine $FeCl_3$ crystallizes in an O1-type layered structure (following Delmas notation)[33], as shown in Fig. 1a, where the $Cl^-$ anions follow an ABAB stacking sequence. Unlike layered compounds with an O3 structure, such as $LiCoO_2$, where each layer is fully filled alternatively with Li and Co octahedra, $FeCl_3$ (or expressed as $Fe_{0.66}Cl_2$) has a much lower cation-to-anion ratio. Therefore, the layers are filled with a combination of $Fe^{3+}$ octahedra and vacant octahedra (in an overall ratio of 2:1), which form a typical in-plane honeycomb ordering pattern (Fig. 1b,c). Two types of stacking schemes along the *c* axis are possible, one with a shift of the honeycomb layer with alternating $Fe^{3+}$ and vacancies along the *c* axis (in space group $R\bar{3}$, as shown in Fig. 1b), whereas the other has honeycomb layers identically stacked along the *c* axis (in space group $P\bar{3}1m$, as shown in Fig. 1c). Pristine $FeCl_3$ possesses the intergrowth of both types of stacking, leading to broad and diffuse scattering peaks in the X-ray diffraction (XRD) and neutron diffraction patterns (Fig. 1d and Supplementary Figs. 1 and 2). A quantitative stacking disorder analysis suggests that the pristine structure contains ~45% of the former stacking ($R\bar{3}$) and ~55% of the latter stacking ($P\bar{3}1m$).

For the $FeCl_3$ solid cells, $Li_{2.75}In_{0.75}Zr_{0.25}Cl_6$ (LIZC) was selected as the SE in the cathode layer because of its good cathode stability and high room-temperature (RT) ionic conductivity (~2 mS $cm^{-1}$)[34,35]. A protective layer of $Li_3YCl_3Br_3$ (LYCB)[32] was used in direct contact with the In–Li anode to avoid the reduction of In and Zr in the LIZC electrolyte. The ionic conductivities of LIZC and LYCB are shown in Supplementary Figs. 3 and 4. The interface resistance between the In–Li alloy and LYCB was evaluated by electrochemical impedance spectroscopy of a Li–In/LYBC/Li–In symmetric cell. The collected Nyquist plot in Supplementary Fig. 5 shows the low interface resistance. The charge/discharge voltage profile of $FeCl_3$ at a rate of 0.1C at RT is shown in Fig. 2a (plotted as voltage versus $Li^+$/Li to facilitate the comparison with other cathodes). An initial discharge capacity of 159 mAh $g^{-1}$ was observed, which is 96% of the theoretical capacity (165 mAh $g^{-1}$, calculated based on the $Fe^{2+}/Fe^{3+}$ redox couple). Two flat plateaux in the range of 3.5–3.8 V are observed, implying that there are possibly two biphasic processes. The average voltage of 3.65 V is much higher than that of lithium iron oxides[36,37] (~2 to 3 V) and higher than that of $LiFePO_4$ (3.42 V)[38]. It is also seemingly higher than the intercalation plateau of $FeF_3$ (3.0–3.3 V)[19]. However, this may be due to the pronounced overpotential in the reactions of $FeF_3$. Recently, experimental[19] and computational[26] investigations have indicated that the equilibrium Li intercalation potential of $FeF_3$ at the initial stage is >3.8 V. With such a high voltage and capacity, the theoretical energy density of $FeCl_3$ is calculated to be 602 Wh $kg^{-1}$, exceeding the theoretical energy density of $LiFePO_4$ (578 Wh $kg^{-1}$). The measured energy density is 558 Wh $kg^{-1}$ (the calculation method for the energy density is described in Methods), which is 92.7% of the theoretical value.

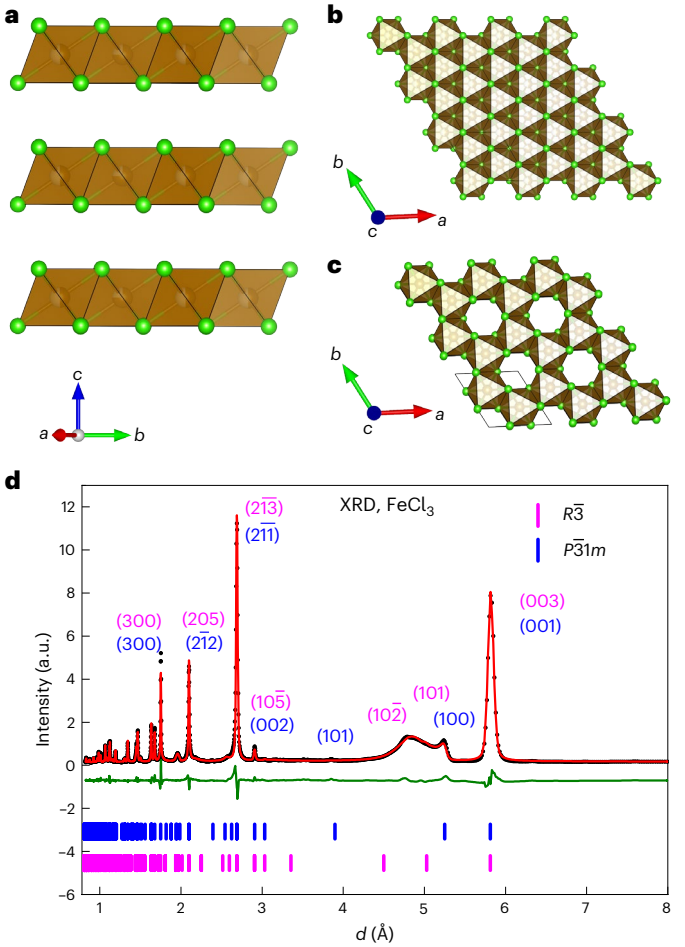


**Fig. 1 | Crystal structure of $FeCl_3$. a**, Side view of the layered structure and the anion stacking of pristine $FeCl_3$. **b**,**c**, There are two different types of stacking of Fe/vacancy honeycomb ordered layers along the *c* axis: alternating stacking (in space group $R\bar{3}$) (**b**) and fully aligned stacking (in space group $P\bar{3}1m$) (**c**). Fe and Cl are shown as brown and green spheres, respectively. **d**, Rietveld refinement against ex situ synchrotron XRD patterns of pristine $FeCl_3$. a.u., arbitrary units.

In the first charging process, the inserted Li ions could be almost fully removed. The charging voltage profile exhibits two flat plateaux. The voltage profiles in successive cycles largely resemble the profile in the first cycle (Fig. 2a), demonstrating good cycling reversibility. The average voltages can be better seen in the corresponding d*Q*/d*V* curves (Fig. 2b). In the first cycle, the two cathodic peaks are centred at 3.56 and 3.67 V (versus $Li^+$/Li), respectively, and the two anodic peaks are at 3.70 and 3.74 V, respectively. In the subsequent cycles, the cathodic peaks shift to higher voltages of 3.58 and 3.68 V, respectively. This observation implies that the electrochemical reaction is highly reversible, although the structural evolution of $FeCl_3$ in the first and successive cycles may be slightly different. Figure 2c,d shows the rate performance of $FeCl_3$ SSLIBs. Figure 2e shows the long-term cyclability of $FeCl_3$ at a rate of 0.5C at RT. After 1,000 cycles, the cell maintained 83% of its initial capacity with an average Coulombic efficiency of 99.98% in each cycle. $FeCl_3$ solid cells with 50 mg cathode loading ($FeCl_3$ 21.71 mg $cm^{-2}$) also exhibit stable cycling with an areal capacity of ~2.5 mAh $cm^{-2}$ at RT (Supplementary Fig. 6). Rate-performance and long-term cycling tests were also performed for $FeCl_3$ SSLIBs at 60 °C, as shown in Supplementary Figs. 7 and 8. $FeCl_3$ SSLIBs exhibit a high capacity of 135 mAh $g^{-1}$ at 1C and a capacity of over 70 mAh $g^{-1}$ at a rate of 5C at 60 °C. Under a higher rate of 2C, the $FeCl_3$ SSLIBs delivered an initial capacity of 115 mAh $g^{-1}$, and a capacity of 70 mAh $g^{-1}$ was maintained after 1,000 cycles (Supplementary Fig. 8), with an average Coulombic efficiency of 99.95% per cycle.

https://doi.org/10.1038/s41893-024-01431-6

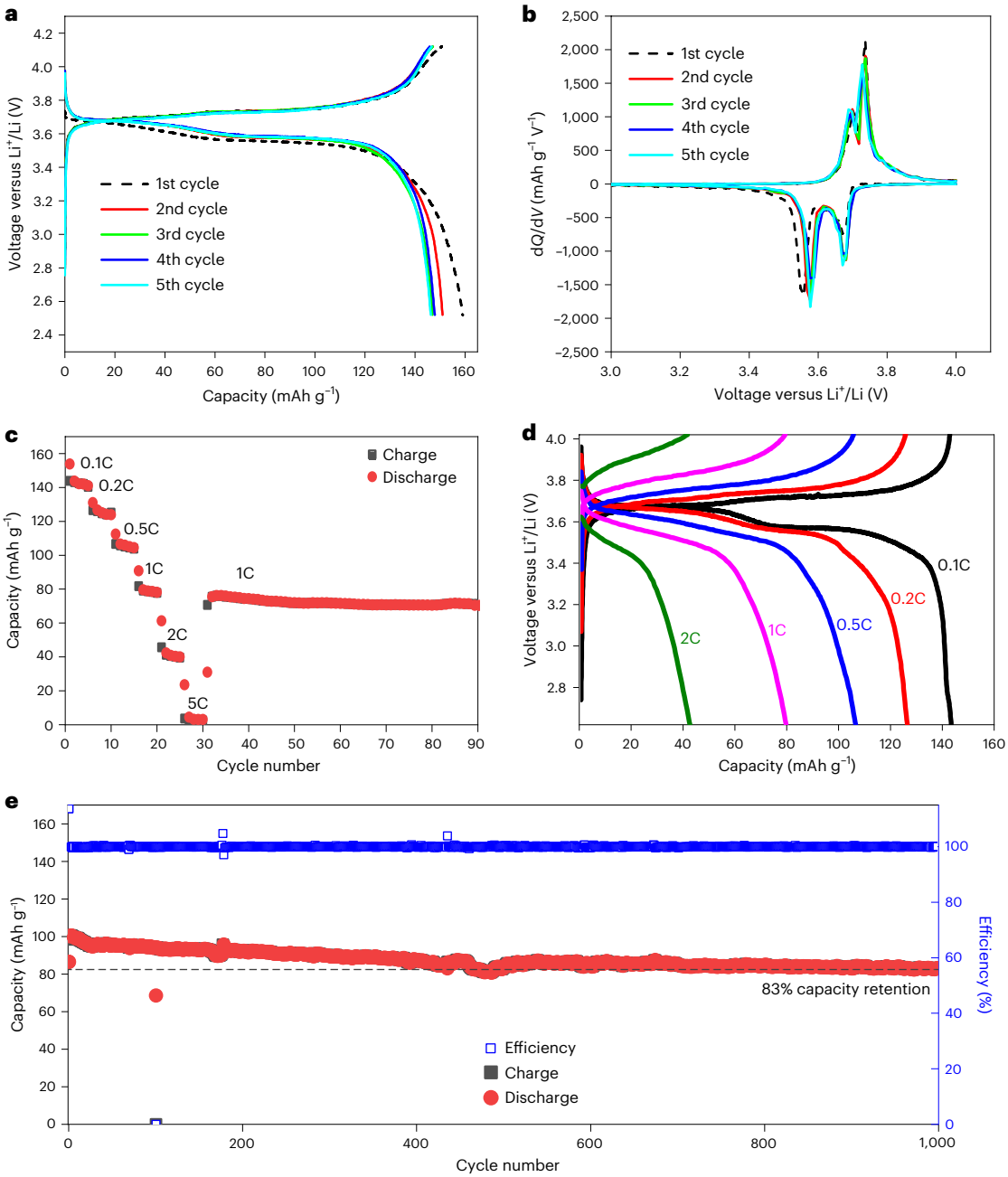


**Fig. 2 | Electrochemical performance of $FeCl_3$ in solid cells. a**, Charge/discharge profile of $FeCl_3$ at a rate of 0.1C at RT with LYCB electrolyte. **b**, Corresponding d$Q$/d$V$ curves. **c**, Rate performance of $FeCl_3$. **d**, Corresponding charge/discharge curves with LIZC/LYCB electrolytes at RT. **e**, Long-term cycling performance of $FeCl_3$ with LIZC/LYCB electrolytes at a rate of 0.5C at RT. The mass loading of $FeCl_3$ was 4.34 mg cm$^{-2}$. The solid cells were cycled between 2.62 and 4.02 V versus $Li^+$/Li at RT.

These results demonstrate the excellent long-term cycling stability of $FeCl_3$ cells at different temperatures and cycling rates.

Ex situ X-ray absorption near edge structure (XANES) data were collected to monitor the change of the oxidation state of Fe during the charging and discharging processes. $FeCl_2$ was used as a reference compound, and its crystal structure is shown in Supplementary Fig. 9. As shown in Fig. 3a,b, starting from pristine $FeCl_3$ and proceeding with more Li inserted, the Fe K edge shifted to lower energy, indicating the reduction of $Fe^{3+}$ to $Fe^{2+}$. When discharged to 2.52 V versus $Li^+$/Li and 0.9 $Li^+$ per formula unit of $FeCl_3$ inserted (blue curve), the Fe K edge shifted so that it almost superposed that of $FeCl_2$ (green curve), in agreement with the electrochemistry data. When the fully discharged $FeCl_3$ was charged back to 4.12 V (noted as $FeCl_3$ after the charging and discharging processes), its Fe K edge shifted back to high energy, close to that of pristine $FeCl_3$, indicating a highly reversible redox of the $Fe^{3+}/Fe^{2+}$ couple.

## Evolution of crystal structure during cycling

To understand the Li insertion and extraction mechanism in $FeCl_3$ during the charging and discharging processes, operando energy-dispersive X-ray diffraction (EDXRD) measurements were performed. These provided structural information from controlled diffraction gauge volumes of tens of micrometres[39]. An all-solid-state cell with an $FeCl_3$/LIZC/carbon composite cathode, LIZC/LYCB bilayer electrolyte and In–Li anode was cycled at a rate of 0.08C at RT. A schematic illustration of the EDXRD set-up is shown in Supplementary Fig. 10. Scans were taken

https://doi.org/10.1038/s41893-024-01431-6

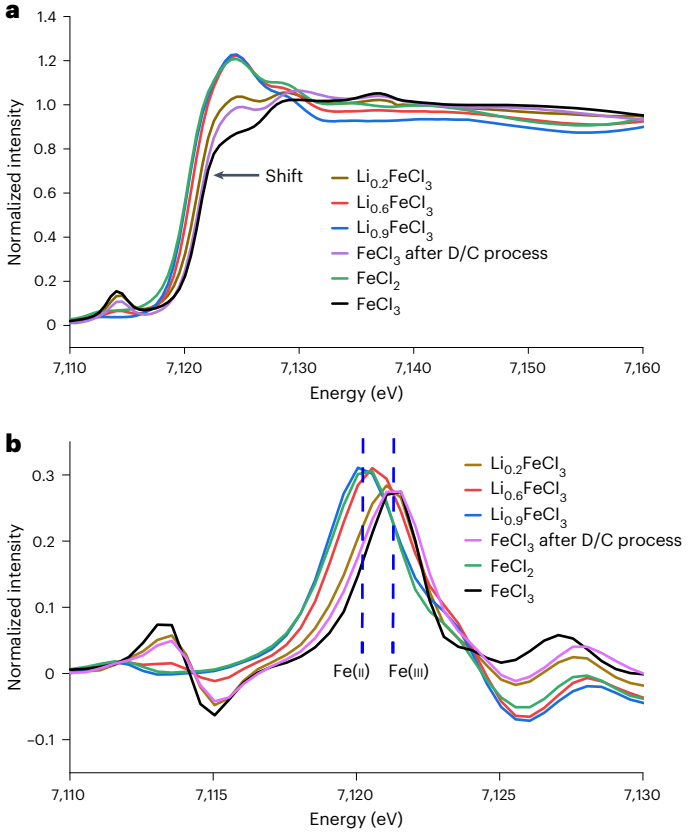


**Fig. 3 | Redox-active element in $FeCl_3$ in the charging and discharging processes. a**, Ex situ Fe K-edge XANES spectra of $FeCl_3$ at different charge/discharge states. **b**, First-order derivatives of Fe K-edge XANES spectra of $FeCl_3$ at different charge and discharge states. $FeCl_2$ is used as a reference. D/C, discharge/charge.

layer by layer along the vertical direction, with an increment of 20 µm. Supplementary Fig. 11 shows a contour plot of the EDXRD patterns of the entire cell before cycling. The span between the two stainless steel rods was ~780 µm, and the cathode thickness was ~100 µm.

Figure 4a shows a contour map of the EDXRD patterns of the cathode layer between 2 and 3.5 Å during the initial charging and discharging processes. The corresponding diffraction patterns are plotted in Supplementary Fig. 12. Reflections at 2.60, 3.02 and 3.15 Å are from electrolyte LIZC in the composite cathode. The strong reflections of $FeCl_3$ at 2.69 Å are assigned to (113) (using space group $R\bar{3}$), and the strong reflections at 2.91 Å are from (006) and (10$\bar{5}$). They do not overlap with reflections from LIZC and thus are used to track the phase evolution of $FeCl_3$.

During the discharge process, two biphasic intercalation processes were observed, like the lithiation process of $VCl_3$ in supersaturated electrolytes[28]. When Li insertion started, reflections from pristine $FeCl_3$ became weaker and an intermediate phase (denoted as the α phase) appeared with a reflection at 2.72 Å at a nominal composition of $Li_{0.2}FeCl_3$. The (113) reflection from $FeCl_3$ disappeared at the nominal composition $Li_{0.35}FeCl_3$, or 3.47 V versus $Li^+$/Li, corresponding to the end of the first flat plateau during the first discharge. The α phase can be indexed using space group $P6_3cm$ (Supplementary Fig. 13). Further Li insertion led to the transformation of the α phase to a more Li-rich phase (denoted as the β phase) with reflections at positions close to LIZC at the end of the discharge process, implying that there was a more significant structural transition at the deep lithiated state. Because the cell used for in situ EDXRD was less optimized than the cell tested in the laboratory, the initial discharge capacity was slightly less (~0.76 Li per formula unit) than in the laboratory data.

During the charging process, the Li-rich the β phase did not transform back to the pristine $FeCl_3$ structure by following the reverse path of lithiation. Instead, a solid-solution delithiation regime between $Li_{0.76}FeCl_3$ and $Li_{0.53}FeCl_3$ was observed, with reflections at 2.60, 3.02 and 3.15 Å shifting to smaller *d*-spacing monotonically at the beginning of the charging process. Further extraction of $Li^+$ led to the formation of a new phase (denoted as the γ phase) with reflections at 2.53 and 2.91 Å. Following that, a second solid-solution regime was observed with further delithiation, corresponding to the plateau at a higher potential in the charge process. The voltages at which the phase transitions were identified are consistent with the voltages observed in the d*Q*/d*V* curves in Fig. 2b. The operando EDXRD patterns are also in good agreement with the ex situ XRD data (Supplementary Fig. 14). Supplementary Fig. 15 is a diagram showing the structural evolution of $FeCl_3$ in solid cells during the initial discharge and charge processes.

To further elucidate the structure of the fully lithiated $FeCl_3$ (β phase), ex situ synchrotron XRD and neutron powder diffraction data were collected. The lithiated $FeCl_3$ was recovered from discharged cells with a cathode mass loading >39 mg $cm^{-2}$. The cathode layer contained only $FeCl_3$ and carbon, so that there was no signal from SEs, which facilitated the analysis of the diffraction data. As shown in Supplementary Fig. 16, at a low current density of 0.063 mA $cm^{-2}$, deep lithiation of $FeCl_3$ (147 mAh $g^{-1}$) was achieved with a $FeCl_3$ mass loading of 78.94 mg $cm^{-2}$ at 60 °C (corresponding to a 100 mg cathode mixture in total, with $FeCl_3$:carbon = 85:15). Supplementary Fig. 13 shows the Rietveld refinement of ex situ synchrotron XRD data for a sample with a nominal formula $Li_{0.4}FeCl_3$ (α phase), which was obtained in the initial discharge process. The crystal structure extracted from the refinement is shown in Supplementary Table 1. After the initial lithiation, the overall anion arrangement changed from predominantly AB… stacking to AB BA BA AB… stacking, as shown in Supplementary Fig. 17. This suggests that the phase transition from the pristine $FeCl_3$ to the α phase is not simply by slabbing of $FeCl_6$ layers. Instead, there was probably partial Fe migration during the lithiation process, leading to the rearrangement of the anion layer. We tentatively assign the inserted $Li^+$ to these octahedral sites (Supplementary Fig. 17c), leading to Li–Cl bond lengths of around 2.6 Å. Further lithiation led to the phase transition from the α to the β phase.

Figure 4b and Supplementary Fig. 18 show the Rietveld refinements of ex situ synchrotron XRD data for a sample with a nominal formula $Li_{0.8}FeCl_3$ and of ex situ neutron diffraction data for a sample with nominal formula $Li_{0.74}FeCl_3$, respectively. The crystal structures extracted from the refinement are shown in Supplementary Tables 2 and 3. Both patterns can be indexed using the *C*2/*m* space group with Cl in an O3-type ABCABC stacking. The structural solution given by a charge flipping algorithm indicates that this new phase crystallizes in the distorted spinel structure, with Fe occupying the spinel octahedral B-sites (Supplementary Fig. 19). Further Rietveld refinement of synchrotron XRD data confirmed that Fe partially occupies the 4*e* site (occupancy refined to be 0.175(3)). Difference Fourier maps generated from neutron diffraction patterns show that Li ions predominately reside on the 4*e* (octahedral) sites with very limited occupation of the 4*g* (tetrahedral) sites (Fig. 4c). The structure can be viewed as a cation-deficient spinel structure, like the high-temperature phase of $LiVCl_3$ (ref. 40). This observation also confirms that during the initial discharge process, Fe partially migrated (both in-plane and out-of-plane) to probably form a thermodynamically more stable spinel-like structure. The transition from the O1-type layered structure to the distorted spinel-like structure (O3-type stacking) during lithiation is probably the reason for the voltage differences between the initial discharge and subsequent cycles (Fig. 2a,b). The structure of the Li-poor γ phase is not fully solved at this point due to the limited quality of the diffraction data. Indexing of the ex situ XRD data (Supplementary Fig. 20) suggests that the unit cell volume is 188.66(30) $Å^3$, slightly larger than that for the pristine $FeCl_3$. In addition, it is probably a

https://doi.org/10.1038/s41893-024-01431-6

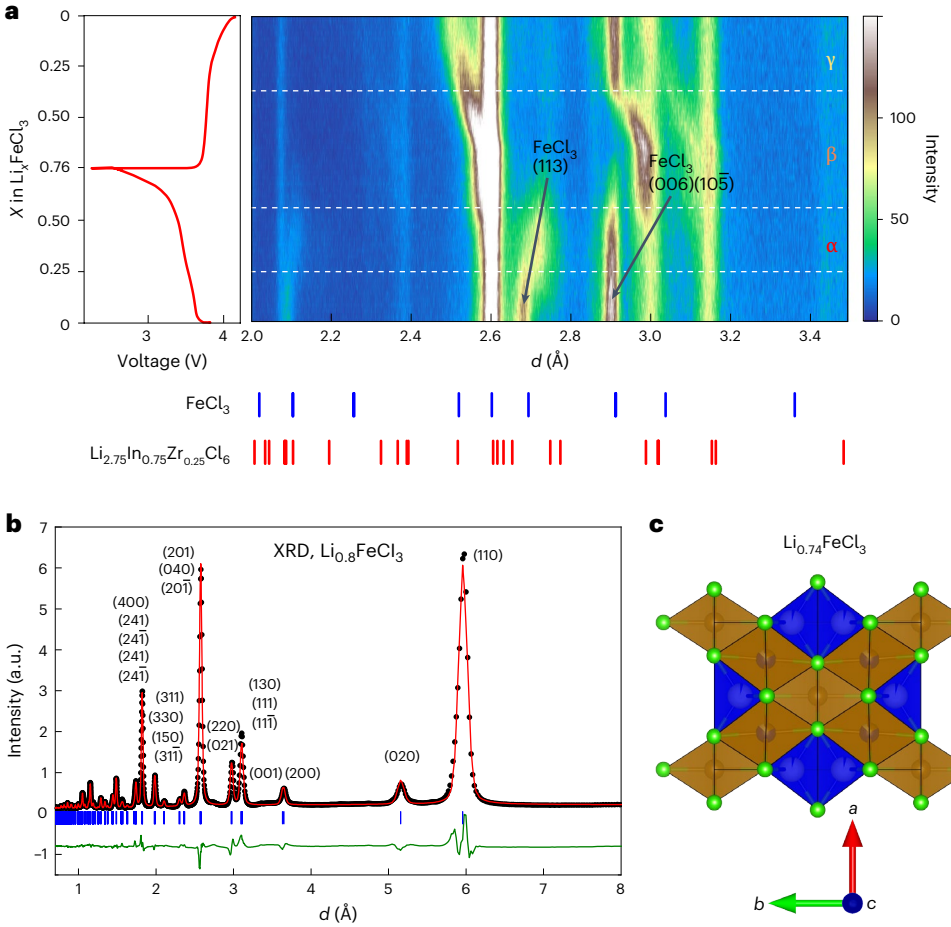


**Fig. 4 | Structural characterization. a**, Contour map between 2 and 3.5 Å of the phase evolution of the cathode during the initial discharging and charging processes and the corresponding voltage profile. **b**, Rietveld refinement of ex situ synchrotron XRD patterns of deeply lithiated $Li_{0.8}FeCl_3$. **c**, Structure of deeply lithiated $FeCl_3$ (β phase) drawn based on the refinement of the synchrotron XRD of $Li_{0.8}FeCl_3$ and neutron diffraction of $Li_{0.74}FeCl_3$. Fe, Cl and Li are shown as brown, green and blue spheres, respectively.

distorted spinel-like structure rather than a layered structure like pristine $FeCl_3$, as the out-of-plane migration of Fe may not be reversible. Although the structure does not return to pristine $FeCl_3$ at the end of the first cycle, the stable long-term cycling data shown in Fig. 2e and Supplementary Fig. 8 imply that the system can stably shuttle between the Li-rich and Li-poor phases during long-term cycling. There are many accessible Li sites for reversible intercalation and deintercalation in the distorted spinel-like structure.

## Discussion

Overall, $FeCl_3$ shows an excellent energy density, rate capability and cycling stability, making it a very promising cathode. Figure 5a compares the voltage, specific capacity and energy density of $FeCl_3$ with several intercalation cathodes that are widely used in commercial LIBs. $FeCl_3$ has a higher voltage (3.65 V versus 3.4 V) than $LiFePO_4$ and a similar theoretical capacity (165 mAh $g^{-1}$ versus 170 mAh $g^{-1}$). It has an overall higher theoretical gravimetric energy density (602 Wh $kg^{-1}$) than $LiFePO_4$ (578 Wh $kg^{-1}$) and $LiMn_2O_4$ (480 Wh $kg^{-1}$). The material-based practical energy density of $FeCl_3$, calculated based on the data obtained in this work, is 558 Wh $kg^{-1}$, which is also higher than the practical energy densities of $LiFePO_4$ (420–550 Wh $kg^{-1}$) and $LiMn_2O_4$ (460–480 Wh $kg^{-1}$). The theoretical density of $FeCl_3$ is 2.9 g $cc^{-1}$, which is lower than that of $LiFePO_4$ (3.58 g $cc^{-1}$). However, $LiFePO_4$ commonly has quite low tap and pack densities (1–2 g $cc^{-1}$). $FeCl_3$, as used in this work, has a rather high pack density of over 2.6 g $cc^{-1}$, as it benefits from the big particles and its intrinsic ductility. The Young's modulus of $FeCl_3$ was measured to be 6.14 ± 0.09 GPa by nano-indentation, indicating that $FeCl_3$ is much softer than most halide[41] and sulfide[42] electrolytes (30–40 GPa). This may help it to form a dense composite cathode with intimate contact between the cathode and electrolyte layer. It is estimated that its material-based volumetric energy density is also very high (>1,500 Wh $L^{-1}$), comparable with cathodes made with lithium nickel manganese cobalt oxides (NMC).

Beyond the excellent electrochemical performance, the next most appealing feature of a $FeCl_3$ cathode is its low cost. Figure 5b summarizes the market prices in May 2022 of $LiCoO_2$, NMC811, $LiMn_2O_4$ (Beijixing, 2022, https://news.bjx.com.cn/html/20220606/1230755.shtml) and $FeCl_3$ (ShengYiShe, 2022, https://www.100ppi.com/mprice/plist-1-1662-1.html). The price of lithium metal oxide cathodes ranged from USD 18,700 ($LiMn_2O_4$) to 79,800 ($LiCoO_2$) per metric tonne. The price of $LiFePO_4$ was also above USD 20,000 per metric tonne. In comparison, the market price of $FeCl_3$ was USD 516 per metric tonne, only ~2% the price of $LiFePO_4$ and ~1% the price of NMC. The cost of $FeCl_3$ was calculated to be USD 0.86 $kWh^{-1}$, which is lower than the cost of current cathodes, which ranged from USD 39 $kWh^{-1}$ to USD 125 $kWh^{-1}$ (Fig. 5c). We also compare the cost of the $FeCl_3$/Li pair with other cathode/anode pairs in commercial LIBs (Supplementary Table 4 and Supplementary Fig. 21). The cost of the $FeCl_3$/Li pair was USD 3.70 $kWh^{-1}$, which is 7.5% of the cost for lithium iron phosphate C and 4.2% of the cost for NMC-C. Compared with several newly developed, promising cathode materials, such as $VCl_3$ (ref. 43), $Li_3TiCl_6$ (ref. 44) and $FeF_2$ (ref. 45), $FeCl_3$ also shows advantages in terms of energy density and cost, as shown in

https://doi.org/10.1038/s41893-024-01431-6

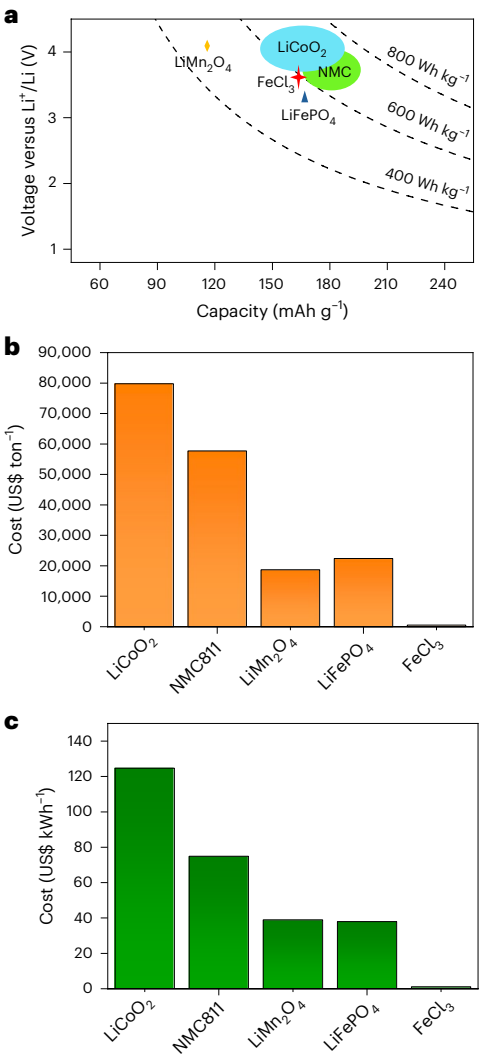


**Fig. 5 | Energy density and cost. a**, Voltage and specific capacity of different cathode materials. **b**, Market prices of different cathode materials. **c**, Calculated cost of cathode materials per kilowatt hour.

Supplementary Tables 5 and 6. For large-scale battery production, expensive Y- and In-containing SEs could be replaced by Zr-based electrolytes (for example, $Li_2ZrCl_6$)[46–48] and a much thinner SE layer could be made using a roll-to-roll process with polymer binders[47,49]. When coupled with anodes such as an Si–Li alloy and Li metal, sulfide electrolytes can be used as the protective layer[50,51]. $Li_2ZrCl_6$ is not stable against $Li_6PS_5Cl$, but their interface can be passivated by fluorination of $Li_2ZrCl_6$ (ref. 52). Cells using $Li_2ZrCl_6$ as the SE were also tested as a proof of concept (Supplementary Fig. 22). The cycling capacity was slightly lower than that of cells with LIZC electrolyte, as shown in Fig. 2, probably due to the lower conductivity of $Li_2ZrCl_6$ (~0.4 mS $cm^{-1}$) compared to LIZC (2 mS $cm^{-1}$). It is expected that the performance of the cell could be optimized after this preliminary test. Supplementary Table 7 lists the estimated costs of $FeCl_3$/Li all-solid-state cells with $Li_2ZrCl_6$ SEs. This table demonstrates the significant cost advantage of $FeCl_3$ cathodes over existing cathode materials. Although the water sensitivity of $FeCl_3$ may slightly increase the cost of storage, handling and transportation, such added cost would be well compensated for and overwhelmed by the cost advantage of $FeCl_3$ over other cathodes. Although all-solid-state batteries are not at present commercialized on large scales and their cost (before and after replacing oxide cathodes by $FeCl_3$) cannot be explicitly formulated like conventional LIBs, it is potentially possible to reduce the cost of LIB cells from the current approximately USD 120–150 $kWh^{-1}$ to USD 50–80 $kWh^{-1}$. This substantial cost reduction could make Li-based solid-state batteries truly economically viable solutions for large-scale energy storage, such as electrical grid storage, which may reshape the energy industries. More importantly, as $FeCl_3$-based battery systems do not use any Co or Ni, they certainly can significantly elevate the sustainability of LIB technologies.

In summary, the reversible insertion and extraction of Li in $FeCl_3$ has been realized. This was enabled using a SE, which critically alleviates the dissolution problem of chlorides. A high energy density of 558 kWh $kg^{-1}$, exceeding that of $LiFePO_4$, together with good rate performance and stable long-term cycling were achieved. XANES, EDXRD and ex situ synchrotron and neutron diffraction revealed that the $FeCl_3$ turned into a spinel-like structure that was highly stable against Li insertion and extraction during long-term cycling. As a new type of cathode material, the high energy density and ultra-low cost make $FeCl_3$ a very promising cathode for next-generation SSLIBs, particularly in large-scale energy storage applications, such as electrified transportation and electric grid energy storage.

## Methods

### Materials synthesis

$Li_{2.75}In_{0.75}Zr_{0.25}Cl_6$ was synthesized by high-energy ball-milling followed by annealing. LiCl (Sigma-Aldrich), $InCl_3$ (Bean Town Chemical, 99.9%) and $ZrCl_4$ (Thermo Scientific Chemicals, 98%) were weighed out in the desired ratio and ball-milled at 500 rpm for 5 h. The ball-milled mixture was pelletized and placed in a sealed quartz tube. The pellet was heated at 425 °C for 5 h, then cooled to RT in a furnace. $Li_3YCl_3Br_3$ was prepared following the same synthesis protocol. LiBr (Sigma-Aldrich) and $YCl_3$ (Sigma-Aldrich) were ball-milled for 5 h followed by sintering. All treatments were done under an argon atmosphere.

### Ex situ synchrotron XRD and neutron powder diffraction

Synchrotron XRD patterns were collected at the synchrotron X-ray source of beamline 17-BM at the Advanced Photon Source and at the 28ID-2 beamline of the National Synchrotron Light Source II. High-quality neutron powder diffraction data were collected at the NOMAD beamline of the Spallation Neutron Source at Oak Ridge National Laboratory. Rietveld refinements of the XRD and neutron powder diffraction data were performed with TOPAS[53]. For the data analysis using neutron diffraction data, time-of-flight data were converted to $d$-spacing data using the polynomial $TOF = ZERO + DIFC \times d + DIFA \times d^2$, where ZERO is a constant, DIFC is the diffractometer constant and DIFA is an empirical term to correct the peak shift due to sample displacement and absorption. During the refinement, ZERO and DIFC were determined from the refinement using NIST Si 640e standard data, whereas DIFA was allowed to vary to account for sample displacement. A back-to-back exponential function convoluted with a symmetrical Gaussian function was used to describe the peak profile.

### Electrochemical measurements

The ionic conductivity was measured with an electrochemical impedance analyser (VMP3, Bio-logic) and a home-made electrochemical cell. Typically, 0.5–1 g of electrolyte powders was cold-pressed into pellets with a diameter of 1/2 inch at a pressure of 294 MPa. Two pieces of Al foil were used as current collectors, and the data were collected at various temperatures in the frequency range from 1 MHz to 1 Hz with an a.c. amplitude of 50 mV.

The all-solid-state cells were fabricated by sandwiching the composite cathode, separator and anode inside a home-made cell frame. The composite cathode contained $FeCl_3$ (Spectrum Chemicals, 98%) as well as synthesized SEs ($Li_{2.75}In_{0.75}Zr_{0.25}Cl_6$) and acetylene black powder. These were mixed in the desired ratio, for example, 55:40:5 (wt%),

in a mortar by hand. In–Li alloy was used as the anode. In–Li alloy with a nominal composition of In50–Li50 was prepared by pressing In and Li metal together at 294 MPa. It was then mixed with LYCB in a weight ratio of 70:30 in a mortar by hand. SE powder was pelletized and used as the separator. In a typical cell fabrication, 120 mg of LIZC powder was placed in a poly(methyl methacrylate) sleeve and pressed at 294 MPa. Then, 80 mg of LYBC was used as a protective layer between the LIZC and anode layer. Next, 10 mg of the $FeCl_3$/LIZC/AB composite cathode mixture was pressed on the LIZC pellet side with a pressure of 294 MPa. Finally, 25 mg of the composite anode mixture was pressed onto the LYCB layer side. $FeCl_3$ samples at different charge and discharge states for ex situ synchrotron and neutron diffraction measurements were recovered from solid cells in which the cathode layer contained only $FeCl_3$ and carbon in a weight ratio of 85:15. The cell used for the operando EDXRD measurements had an LIZC electrolyte, with a composite cathode mass loading of 25 mg and composite anode mass loading of 50 mg. Cycling was conducted at RT in galvanostatic mode between 1.9 and 3.5 V versus In–Li. The energy density of $FeCl_3$ was calculated by integrating the voltage versus capacity. The energy density of the other electrode materials was estimated from the product of their average voltage and capacity.

### Operando EDXRD

Operando EDXRD measurements were conducted at the 6-BM-A beamline at the Advanced Photon Source in Argonne National Lab. The incident beam size was 2.00 mm × 0.020 mm, and the receiving slit sizes were 4.00 mm × 0.20 mm. A germanium detector was fixed at 2.301084° to measure the intensity of the diffracted beam. The vertical length of an all-solid-state cell was scanned layer by layer with a step size of 20 µm. The data acquisition time was 30 s, and a Savitzky–Golay filter was used to smooth the data.

### X-ray absorption near edge structure

The change of the oxidation state of Fe during discharging and charging was examined by synchrotron Fe K-edge X-ray absorption spectroscopy, which was conducted at Beamline 12-BM-B at the Advanced Photon Source, Argonne National Laboratory. Sample solids were loaded into epoxy-sealed Kapton capillary tubes in an Ar atmosphere. XANES data were then collected. The energy was calibrated with Fe foil. Each sample underwent several scans (4–6), and the data were averaged and normalized. The Fe XANES data analysis was performed with Athena[54].

### Reporting summary

Further information on research design is available in the Nature Portfolio Reporting Summary linked to this article.

## Data availability

All data in this work are available in the text and Supplementary Information. Source data are provided with this paper.

## References


1. Janek, J. & Zeier, W. G. A solid future for battery development. *Nat. Energy* **1**, 16141 (2016).
2. Lu, J., Wu, T. & Amine, K. State-of-the-art characterization techniques for advanced lithium-ion batteries. *Nat. Energy* **2**, 17011 (2017).
3. Yang, Z., Huang, H. & Lin, F. Sustainable electric vehicle batteries for a sustainable world: perspectives on battery cathodes, environment, supply chain, manufacturing, life cycle, and policy. *Adv. Energy Mater.* **12**, 2200383 (2022).
4. Zhang, Z.-j et al. Polypyrrole-coated α-$LiFeO_2$ nanocomposite with enhanced electrochemical properties for lithium-ion batteries. *Electrochim. Acta* **108**, 820–826 (2013).
5. Chung, S.-Y., Bloking, J. T. & Chiang, Y.-M. Electronically conductive phospho-olivines as lithium storage electrodes. *Nat. Mater.* **1**, 123–128 (2002).
6. Kang, B. & Ceder, G. Battery materials for ultrafast charging and discharging. *Nature* **458**, 190–193 (2009).
7. Fang, S., Bresser, D. & Passerini, S. Transition metal oxide anodes for electrochemical energy storage in lithium- and sodium-ion batteries. *Adv. Energy Mater.* **10**, 1902485 (2020).
8. Zhong, K. et al. Investigation on porous MnO microsphere anode for lithium ion batteries. *J. Power Sources* **196**, 6802–6808 (2011).
9. He, K. et al. Transitions from near-surface to interior redox upon lithiation in conversion electrode materials. *Nano Lett.* **15**, 1437–1444 (2015).
10. Hua, X. et al. Comprehensive study of the $CuF_2$ conversion reaction mechanism in a lithium ion battery. *J. Phys. Chem. C* **118**, 15169–15184 (2014).
11. Liu, J.-L., Cui, W.-J., Wang, C.-X. & Xia, Y.-Y. Electrochemical reaction of lithium with $CoCl_2$ in nonaqueous electrolyte. *Electrochem. Commun.* **13**, 269–271 (2011).
12. Xiao, A. W. et al. Understanding the conversion mechanism and performance of monodisperse $FeF_2$ nanocrystal cathodes. *Nat. Mater.* **19**, 644–654 (2020).
13. Li, T., Chen, Z. X., Cao, Y. L., Ai, X. P. & Yang, H. X. Transition-metal chlorides as conversion cathode materials for Li-ion batteries. *Electrochim. Acta* **68**, 202–205 (2012).
14. Karki, K. et al. Revisiting conversion reaction mechanisms in lithium batteries: lithiation-driven topotactic transformation in $FeF_2$. *J. Am. Chem. Soc.* **140**, 17915–17922 (2018).
15. Wu, F. et al. Metal–organic framework-derived nanoconfinements of $CoF_2$ and mixed-conducting wiring for high-performance metal fluoride-lithium battery. *ACS Nano* **15**, 1509–1518 (2021).
16. Chang, D., Chen, M.-H. & Van der Ven, A. Factors contributing to path hysteresis of displacement and conversion reactions in Li ion batteries. *Chem. Mater.* **27**, 7593–7600 (2015).
17. Cabana, J., Monconduit, L., Larcher, D. & Palacín, M. R. Beyond intercalation-based Li-ion batteries: the state of the art and challenges of electrode materials reacting through conversion reactions. *Adv. Mater.* **22**, E170–E192 (2010).
18. Wang, F. et al. Tracking lithium transport and electrochemical reactions in nanoparticles. *Nat. Commun.* **3**, 1201 (2012).
19. Hua, X. et al. Revisiting metal fluorides as lithium-ion battery cathodes. *Nat. Mater.* **20**, 841–850 (2021).
20. Liu, P., Vajo, J. J., Wang, J. S., Li, W. & Liu, J. Thermodynamics and kinetics of the Li/$FeF_3$ reaction by electrochemical analysis. *J. Phys. Chem. C* **116**, 6467–6473 (2012).
21. Fu, W. et al. Iron fluoride–carbon nanocomposite nanofibers as free-standing cathodes for high-energy lithium batteries. *Adv. Funct. Mater.* **28**, 1801711 (2018).
22. Wiaderek, K. M. et al. Comprehensive insights into the structural and chemical changes in mixed-anion FeOF electrodes by using operando PDF and NMR spectroscopy. *J. Am. Chem. Soc.* **135**, 4070–4078 (2013).
23. Jung, S.-K. et al. New iron-based intercalation host for lithium-ion batteries. *Chem. Mater.* **30**, 1956–1964 (2018).
24. Ko, J. K. et al. Transport, phase reactions, and hysteresis of iron fluoride and oxyfluoride conversion electrode materials for lithium batteries. *ACS Appl. Mater. Interfaces* **6**, 10858–10869 (2014).
25. Kim, T. et al. A cathode material for lithium-ion batteries based on graphitized carbon-wrapped $FeF_3$ nanoparticles prepared by facile polymerization. *J. Mater. Chem. A* **4**, 14857–14864 (2016).
26. Li, L. et al. Origins of large voltage hysteresis in high-energy-density metal fluoride lithium-ion battery conversion electrodes. *J. Am. Chem. Soc.* **138**, 2838–2848 (2016).
27. Wu, F. & Yushin, G. Conversion cathodes for rechargeable lithium and lithium-ion batteries. *Energy Environ. Sci.* **10**, 435–459 (2017).

28. Dubouis, N. et al. Extending insertion electrochemistry to soluble layered halides with superconcentrated electrolytes. *Nat. Mater.* **20**, 1545–1550 (2021).
29. Asano, T. et al. Solid halide electrolytes with high lithium-ion conductivity for application in 4 V class bulk-type all-solid-state batteries. *Adv. Mater.* **30**, 1803075 (2018).
30. Park, K.-H. et al. High-voltage superionic halide solid electrolytes for all-solid-state Li-ion batteries. *ACS Energy Lett*. **5**, 533–539 (2020).
31. Li, X. et al. Air-stable $Li_3InCl_6$ electrolyte with high voltage compatibility for all-solid-state batteries. *Energy Environ. Sci.* **12**, 2665–2671 (2019).
32. Liu, Z. et al. High ionic conductivity achieved in $Li_3Y(Br_3Cl_3)$ mixed halide solid electrolyte via promoted diffusion pathways and enhanced grain boundary. *ACS Energy Lett.* **6**, 298–304 (2021).
33. Delmas, C., Fouassier, C. & Hagenmuller, P. Structural classification and properties of the layered oxides. *Phys. B+C* **99**, 81–85 (1980).
34. Helm, B. et al. Exploring aliovalent substitutions in the lithium halide superionic conductor $Li_{3-x}In_{1-x}Zr_xCl_6$ ($0 \le x \le 0.5$). *Chem. Mater.* **33**, 4773–4782 (2021).
35. Kwak, H. et al. $Li^+$ conduction in aliovalent-substituted monoclinic $Li_2ZrCl_6$ for all-solid-state batteries: $Li_{2+x}Zr_{1-x}M_xCl_6$ (M=In, Sc). *J. Chem. Eng.* **437**, 135413 (2022).
36. Kanno, R. et al. Synthesis, structure, and electrochemical properties of a new lithium iron oxide, $LiFeO_2$, with a corrugated layer structure. *J. Electrochem. Soc.* **143**, 2435–2442 (1996).
37. Kanno, R., Shirane, T., Inaba, Y. & Kawamoto, Y. Synthesis and electrochemical properties of lithium iron oxides with layer-related structures. *J. Power Sources* **68**, 145–152 (1997).
38. Padhi, A. K., Nanjundaswamy, K. S. & Goodenough, J. B. Phospho-olivines as positive-electrode materials for rechargeable lithium batteries. *J. Electrochem. Soc.* **144**, 1188–1194 (1997).
39. Sun, X. et al. Operando EDXRD study of all-solid-state lithium batteries coupling thioantimonate superionic conductors with metal sulfide. *Adv. Energy Mater.* **11**, 2002861 (2021).
40. Soubeyroux, J. L., Cros, C., Gang, W., Kanno, R. & Pouchard, M. Neutron diffraction investigation of the cationic distribution in the structure of the spinel-type solid solutions $Li_{2-2x}M_{1+x}Cl_4$ (M=Mg, V): correlation with the ionic conductivity and NMR data. *Solid State Ion.* **15**, 293–300 (1985).
41. Jiang, M. et al. Materials perspective on new lithium chlorides and bromides: insights into thermo-physical properties. *Phys. Chem. Chem. Phys.* **22**, 22758–22767 (2020).
42. Papakyriakou, M. et al. Mechanical behavior of inorganic lithium-conducting solid electrolytes. *J. Power Sources* **516**, 230672 (2021).
43. Liang, J. et al. Halide layer cathodes for compatible and fast-charged halides-based all-solid-state Li metal batteries. *Angew. Chem. Int. Ed.* **62**, e202217081 (2023).
44. Wang, K., Gu, Z., Xi, Z., Hu, L. & Ma, C. $Li_3TiCl_6$ as ionic conductive and compressible positive electrode active material for all-solid-state lithium-based batteries. *Nat. Commun.* **14**, 1396 (2023).
45. Fan, X. et al. High energy-density and reversibility of iron fluoride cathode enabled via an intercalation-extrusion reaction. *Nat. Commun.* **9**, 2324 (2018).
46. Wang, K. et al. A cost-effective and humidity-tolerant chloride solid electrolyte for lithium batteries. *Nat. Commun.* **12**, 4410 (2021).
47. Kwak, H. et al. Emerging halide superionic conductors for all-solid-state batteries: design, synthesis, and practical applications. *ACS Energy Lett.* **7**, 1776–1805 (2022).
48. Kwak, H. et al. New cost-effective halide solid electrolytes for all-solid-state batteries: mechanochemically prepared $Fe^{3+}$-substituted $Li_2ZrCl_6$. *Adv. Energy Mater.* **11**, 2003190 (2021).
49. Wang, C. et al. Solvent-free approach for interweaving freestanding and ultrathin inorganic solid electrolyte membranes. *ACS Energy Lett.* **7**, 410–416 (2022).
50. Ye, L. & Li, X. A dynamic stability design strategy for lithium metal solid state batteries. *Nature* **593**, 218–222 (2021).
51. Tan, D. H. S. et al. Carbon-free high-loading silicon anodes enabled by sulfide solid electrolytes. *Science* **373**, 1494–1499 (2021).
52. Kwak, H. et al. Boosting the interfacial superionic conduction of halide solid electrolytes for all-solid-state batteries. *Nat. Commun.* **14**, 2459 (2023).
53. Perl, J., Shin, J., Schümann, J., Faddegon, B. & Paganetti, H. TOPAS: an innovative proton Monte Carlo platform for research and clinical applications. *Med. Phys.* **39**, 6818–6837 (2012).
54. Ravel, B. & Newville, M. ATHENA, ARTEMIS, HEPHAESTUS: data analysis for X-ray absorption spectroscopy using IFEFFIT. *J. Synchrotron Radiat.* **12**, 537–541 (2005).


## Acknowledgements

Z.L. and H.C. acknowledge financial support from the National Science Foundation (Grant Nos. 1706723 and 2108688) and from the faculty startup fund of Georgia Tech. The Advanced Photon Source at Argonne National Laboratory was made available through the General User Program, which is supported by the US Department of Energy (DOE), Office of Science, Office of Basic Energy Sciences (Contract No. DE-AC02-06CH11357). This research also used the 28ID-2 XPD beamline of the National Synchrotron Light Source II, a DOE, Office of Science user facility operated for the DOE Office of Science by Brookhaven National Laboratory (Contract No. DE-SC0012704). A portion of this research used resources at the Spallation Neutron Source, a DOE Office of Science user facility operated by Oak Ridge National Laboratory. J.L. thanks the DOE, Office of Science, Office of Basic Energy Sciences for funding support (Grant No. DOE-BES-ERKCSNX). S.Z. and Y.T. acknowledge support from the National Science Foundation (Grant No. 1923802) and NASA (Grant No. 80NSSC21K0483). We thank the beamline scientists J. Okasinski, J. Bai and W. Xu for their help with the synchrotron experiments. We thank Z. Fan's group at the University of Houston for assisting with scanning electron microscopy characterizations.

## Author contributions

Z.L. and H.C. conceived the ideas and designed the experiments. Z.L conducted the synthesis, electrochemical testing and part of the characterizations. J.L. S.Z., S.X., P.B., S.C. and Y.T. contributed to the characterization of materials. J.L. contributed to the structure analysis and wrote part of the manuscript. Z.L., T.Z. and H.C. wrote the manuscript. All authors reviewed and revised the manuscript.

## Competing interests

Z.L. and H.C. have filed a US provisional patent application (63/363,875) covering the application of $FeCl_3$ and related compounds as cathode materials in solid-state batteries as described in this paper. The remaining authors declare no competing interests.

## Additional information

**Supplementary information** The online version contains supplementary material available at https://doi.org/10.1038/s41893-024-01431-6.

**Correspondence and requests for materials** should be addressed to Hailong Chen.

**Peer review information** *Nature Sustainability* thanks the anonymous reviewers for their contribution to the peer review of this work.

nature portfolio

Corresponding author(s): Hailong Chen

Last updated by author(s): 08/02/2024

# Reporting Summary

Nature Portfolio wishes to improve the reproducibility of the work that we publish. This form provides structure for consistency and transparency in reporting. For further information on Nature Portfolio policies, see our Editorial Policies and the Editorial Policy Checklist.

Please do not complete any field with "not applicable" or n/a. Refer to the help text for what text to use if an item is not relevant to your study.
For final submission: please carefully check your responses for accuracy; you will not be able to make changes later.

## Statistics

For all statistical analyses, confirm that the following items are present in the figure legend, table legend, main text, or Methods section.

| n/a | Confirmed | |
|---|---|---|
| [X] | [ ] | The exact sample size (*n*) for each experimental group/condition, given as a discrete number and unit of measurement |
| [X] | [ ] | A statement on whether measurements were taken from distinct samples or whether the same sample was measured repeatedly |
| [X] | [ ] | The statistical test(s) used AND whether they are one- or two-sided<br>*Only common tests should be described solely by name; describe more complex techniques in the Methods section.* |
| [X] | [ ] | A description of all covariates tested |
| [X] | [ ] | A description of any assumptions or corrections, such as tests of normality and adjustment for multiple comparisons |
| [X] | [ ] | A full description of the statistical parameters including central tendency (e.g. means) or other basic estimates (e.g. regression coefficient) AND variation (e.g. standard deviation) or associated estimates of uncertainty (e.g. confidence intervals) |
| [X] | [ ] | For null hypothesis testing, the test statistic (e.g. *F*, *t*, *r*) with confidence intervals, effect sizes, degrees of freedom and *P* value noted<br>*Give P values as exact values whenever suitable.* |
| [X] | [ ] | For Bayesian analysis, information on the choice of priors and Markov chain Monte Carlo settings |
| [X] | [ ] | For hierarchical and complex designs, identification of the appropriate level for tests and full reporting of outcomes |
| [X] | [ ] | Estimates of effect sizes (e.g. Cohen's *d*, Pearson's *r*), indicating how they were calculated |

*Our web collection on statistics for biologists contains articles on many of the points above.*

## Software and code

Policy information about availability of computer code

Data collection: LandMon V7, EC-Lab (V 11.43)

Data analysis: TOPAS (V6), Origin 2023, Vesta (V 3.5.7), Athena (0.9.26)

For manuscripts utilizing custom algorithms or software that are central to the research but not yet described in published literature, software must be made available to editors and reviewers. We strongly encourage code deposition in a community repository (e.g. GitHub). See the Nature Portfolio guidelines for submitting code & software for further information.

## Data

Policy information about availability of data

All manuscripts must include a data availability statement. This statement should provide the following information, where applicable:

- Accession codes, unique identifiers, or web links for publicly available datasets
- A description of any restrictions on data availability
- For clinical datasets or third party data, please ensure that the statement adheres to our policy

All data in this work are available in the text and Supplementary Information. The relevant raw data are listed in Excel documents and provided as source or supplementary data files.

## Research involving human participants, their data, or biological material

Policy information about studies with human participants or human data. See also policy information about sex, gender (identity/presentation), and sexual orientation and race, ethnicity and racism.

| | |
|---|---|
| Reporting on sex and gender | N/A. The study did not involve human research participants. |
| Reporting on race, ethnicity, or other socially relevant groupings | N/A. The study did not involve human research participants. |
| Population characteristics | N/A. The study did not involve human research participants. |
| Recruitment | N/A. The study did not involve human research participants. |
| Ethics oversight | N/A. The study did not involve human research participants. |

Note that full information on the approval of the study protocol must also be provided in the manuscript.

# Field-specific reporting

Please select the one below that is the best fit for your research. If you are not sure, read the appropriate sections before making your selection.

☐ Life sciences ☐ Behavioural & social sciences ☒ Ecological, evolutionary & environmental sciences

For a reference copy of the document with all sections, see nature.com/documents/nr-reporting-summary-flat.pdf

# Life sciences study design

All studies must disclose on these points even when the disclosure is negative.

| | |
|---|---|
| Sample size | N/A |
| Data exclusions | N/A |
| Replication | N/A |
| Randomization | N/A |
| Blinding | N/A |

# Behavioural & social sciences study design

All studies must disclose on these points even when the disclosure is negative.

| | |
|---|---|
| Study description | N/A |
| Research sample | N/A |
| Sampling strategy | N/A |
| Data collection | N/A |
| Timing | N/A |
| Data exclusions | N/A |
| Non-participation | N/A |
| Randomization | N/A |

# Ecological, evolutionary & environmental sciences study design

All studies must disclose on these points even when the disclosure is negative.

| | |
|---|---|
| Study description | The investigation of ferric chloride as the cathode in solid-state Li-ion batteries |
| Research sample | Ferric chloride |
| Sampling strategy | N/A. |
| Data collection | See "Methods" section. |
| Timing and spatial scale | The study was conducted at random times and in fixed laboratories. |
| Data exclusions | No data were excluded from the analyses. |
| Reproducibility | All experiments were repeated several times and the results showed good reproducibility. |
| Randomization | N/A. |
| Blinding | N/A. |

Did the study involve field work? ☐ Yes ☐ No

## Field work, collection and transport

| | |
|---|---|
| Field conditions | N/A. |
| Location | N/A. |
| Access & import/export | N/A. |
| Disturbance | N/A. |

# Reporting for specific materials, systems and methods

We require information from authors about some types of materials, experimental systems and methods used in many studies. Here, indicate whether each material, system or method listed is relevant to your study. If you are not sure if a list item applies to your research, read the appropriate section before selecting a response.

### Materials & experimental systems

| n/a | Involved in the study |
|---|---|
| [X] | [ ] Antibodies |
| [X] | [ ] Eukaryotic cell lines |
| [X] | [ ] Palaeontology and archaeology |
| [X] | [ ] Animals and other organisms |
| [X] | [ ] Clinical data |
| [X] | [ ] Dual use research of concern |
| [X] | [ ] Plants |

### Methods

| n/a | Involved in the study |
|---|---|
| [X] | [ ] ChIP-seq |
| [X] | [ ] Flow cytometry |
| [X] | [ ] MRI-based neuroimaging |

## Antibodies

| | |
|---|---|
| Antibodies used | N/A. |
| Validation | N/A. |

## Eukaryotic cell lines

Policy information about cell lines and Sex and Gender in Research

| | |
|---|---|
| Cell line source(s) | N/A. |
| Authentication | N/A. |
| Mycoplasma contamination | N/A. |
| Commonly misidentified lines (See ICLAC register) | N/A. |

## Palaeontology and Archaeology

| | |
|---|---|
| Specimen provenance | N/A. |
| Specimen deposition | N/A. |
| Dating methods | N/A. |

☐ Tick this box to confirm that the raw and calibrated dates are available in the paper or in Supplementary Information.

| | |
|---|---|
| Ethics oversight | N/A. |

Note that full information on the approval of the study protocol must also be provided in the manuscript.

## Animals and other research organisms

Policy information about studies involving animals; ARRIVE guidelines recommended for reporting animal research, and Sex and Gender in Research

| | |
|---|---|
| Laboratory animals | N/A. |
| Wild animals | N/A. |
| Reporting on sex | N/A. |
| Field-collected samples | N/A. |
| Ethics oversight | N/A. |

Note that full information on the approval of the study protocol must also be provided in the manuscript.

## Clinical data

Policy information about clinical studies

All manuscripts should comply with the ICMJE guidelines for publication of clinical research and a completed CONSORT checklist must be included with all submissions.

| | |
|---|---|
| Clinical trial registration | N/A. |
| Study protocol | N/A. |
| Data collection | N/A. |
| Outcomes | N/A. |

## Dual use research of concern

Policy information about dual use research of concern

### Hazards

Could the accidental, deliberate or reckless misuse of agents or technologies generated in the work, or the application of information presented in the manuscript, pose a threat to:

| No | Yes | |
|---|---|---|
| X | ☐ | Public health |
| X | ☐ | National security |
| X | ☐ | Crops and/or livestock |
| X | ☐ | Ecosystems |
| X | ☐ | Any other significant area |

### Experiments of concern

Does the work involve any of these experiments of concern:

| No | Yes | |
|---|---|---|
| X | ☐ | Demonstrate how to render a vaccine ineffective |
| X | ☐ | Confer resistance to therapeutically useful antibiotics or antiviral agents |
| X | ☐ | Enhance the virulence of a pathogen or render a nonpathogen virulent |
| X | ☐ | Increase transmissibility of a pathogen |
| X | ☐ | Alter the host range of a pathogen |
| X | ☐ | Enable evasion of diagnostic/detection modalities |
| X | ☐ | Enable the weaponization of a biological agent or toxin |
| X | ☐ | Any other potentially harmful combination of experiments and agents |

## Plants

Seed stocks: N/A.

Novel plant genotypes: N/A.

Authentication: N/A.

## ChIP-seq

### Data deposition

☐ Confirm that both raw and final processed data have been deposited in a public database such as GEO.

☐ Confirm that you have deposited or provided access to graph files (e.g. BED files) for the called peaks.

Data access links
*May remain private before publication.*

Files in database submission

Genome browser session
(e.g. UCSC)

### Methodology

Replicates

Sequencing depth

Antibodies

Peak calling parameters

Data quality

Software

## Flow Cytometry

### Plots

Confirm that:

☐ The axis labels state the marker and fluorochrome used (e.g. CD4-FITC).

☐ The axis scales are clearly visible. Include numbers along axes only for bottom left plot of group (a 'group' is an analysis of identical markers).

☐ All plots are contour plots with outliers or pseudocolor plots.

☐ A numerical value for number of cells or percentage (with statistics) is provided.

### Methodology

Sample preparation

Instrument

Software

Cell population abundance

Gating strategy

☐ Tick this box to confirm that a figure exemplifying the gating strategy is provided in the Supplementary Information.

## Magnetic resonance imaging

### Experimental design

Design type

Design specifications

Behavioral performance measures

Imaging type(s)

Field strength

Sequence & imaging parameters

Area of acquisition

Diffusion MRI ☐ Used ☐ Not used

### Preprocessing

Preprocessing software

Normalization

Normalization template

Noise and artifact removal

Volume censoring

### Statistical modeling & inference

Model type and settings

Effect(s) tested

Specify type of analysis: ☐ Whole brain ☐ ROI-based ☐ Both

Statistic type for inference

(See Eklund et al. 2016)

Correction

## Models & analysis

| n/a | Involved in the study |
|---|---|
| ☐ | ☐ Functional and/or effective connectivity |
| ☐ | ☐ Graph analysis |
| ☐ | ☐ Multivariate modeling or predictive analysis |

Functional and/or effective connectivity

Graph analysis

Multivariate modeling and predictive analysis